

## Supplementary Information

### **Creation and Modulation of Ferromagnetism in Antiferromagnetic Hematite Nanoplates**

Jiayi Li<sup>1</sup>, Zihan Wang<sup>1</sup>, Sen Li<sup>2</sup>, Chu Ye<sup>2</sup>, Daojiang Gao<sup>1</sup>, Jiangtao Wu<sup>\*1</sup>,  
Guoping Zhao<sup>\*2</sup> and Zuo-Guang Ye<sup>\*3</sup>

*<sup>1</sup>College of Chemistry and Materials Science, Sichuan Normal University, Chengdu  
610068, China*

*<sup>2</sup>College of Physics and Electronic Engineering, Sichuan Normal University,  
Chengdu 610068, China*

*<sup>3</sup>Department of Chemistry&4D LABS, Simon Fraser University, Burnaby, BC, V5A  
1S6, Canada*

Corresponding author E-mail: [jtwu@sicnu.edu.cn](mailto:jtwu@sicnu.edu.cn); [zhaogp@uestc.edu.cn](mailto:zhaogp@uestc.edu.cn); [zye@sfu.ca](mailto:zye@sfu.ca)

#### **S1: Saturation magnetization calculation.**

The saturation magnetization of the {001} sample can be attributed to a large number of uncompensated spins on the surface and the bulk magnetization in  $\alpha$ -Fe<sub>2</sub>O<sub>3</sub> (250 K < T < 900 K):

$$M_s = \frac{N_{Fe}M_{Fe}}{2\rho v}, \quad (1)$$

where,  $N_{Fe}$  denotes the uncompensated number of Fe atoms in each particle, contributing to the FM magnetization of the sample,  $M_{Fe} = 5.9 \mu_B$  is the magnetic

contribution from each Fe atom (high spin) with where  $1 \mu_B = 9.273 \times 10^{-21}$  erg/Oe.  $5.256 \text{ g/cm}^3$  is the density of  $\alpha\text{-Fe}_2\text{O}_3$  and  $v$  is the volume of each particle. A factor of  $1/2$  is added because statistically, only those half particles (with odd number of Fe layers) in the [001] direction will contribute to one layer of uncompensated Fe atoms, whereas for those with even number of layers, the magnetic moments of Fe atoms are canceled each other.

$$N_{Fe} = 2\gamma S, \quad (2)$$

where,  $\gamma$  is the iron atom density of the termination layer (for the {001} facets,  $\gamma$  is  $4.6 \text{ atoms/nm}^2$ ) and  $S$  is the surface area of each particle. A factor of 2 is added because there are two layer of un-canceled  $\text{Fe}^{3+}$  atom on the surface. Eq. (1) can be rewritten as:

$$M_s = \frac{2\gamma S M_{Fe}}{2\rho S d} = \frac{\gamma M_{Fe}}{\rho d}, \quad (3)$$

where,  $d$  is the thickness of each particle. Using the data mentioned above,  $M_s$  is calculated to be:

$$M_s (\text{emu.g}^{-1}) = 47.9/d(\text{nm}). \quad (4)$$

Thus, the saturation magnetization is approximately inversely proportional to the thickness  $d$  of the {001} samples.

## S2 VAMPIRE simulation

In this work, we use the open source atomistic simulator Vampire for the modeling of the  $\alpha$ -Fe<sub>2</sub>O<sub>3</sub> nanoplates. We adopt the following continuum-scale parameters from<sup>2, 3</sup> with  $M_s = 1.84 \times 10^6$  A.m<sup>-1</sup>,  $K_u = 2.0 \times 10^3$  J.m<sup>-3</sup>,  $T_N = 950$  K, where the sublattice magnetization  $M_1 = M_2 = 9.2 \times 10^5$  A.m<sup>-1</sup>. Taking the directional unit cell parameters  $a = b = 0.504$  nm and  $c = 0.229$  nm (Fig. S1). Thus, the atomic-scale parameters can be

derived as

$$\mu_s = \frac{M_s V}{n_{at}} = 5.76 \mu_B, \quad k_u = \frac{K_u V}{n_{at}} = 5.8 \times 10^{-24} \text{J/atom},$$

$$J_{inter} = -\frac{3k_B T_N}{\epsilon z} = -6.42 \times 10^{-21} \text{J/link} \quad \text{and} \quad J_{intra} = -\frac{2J_{inter}}{3} = 4.28 \times 10^{-21} \text{J/link}.$$

Here  $V$  is the

volume of the unit cell, the number of nearest neighbors  $z = 8$ , the number of atoms per unit cell  $n_{at} = 2$ ,  $J_{inter}$  is the interface exchange coupling constant,  $J_{intra}$  is the intra-layer exchange constant, and the spin-wave MF (mean-field) correction factor<sup>4</sup>  $\epsilon = 0.766$ . Furthermore, because the present work focuses on the saturation magnetization of the nanoparticles rather than their dynamical properties, a damping factor of  $\alpha = 0.1$  is used. In the simulation, we also add a factor of 1/2 because statistically, only those half particles (with odd number of Fe layers) in the [001] direction will contribute to one layer of uncompensated Fe atoms, whereas for those with even number of layers, the magnetic moments of Fe atoms are canceled each other. The simulated values of saturation magnetization with various thicknesses are given in Table S1.

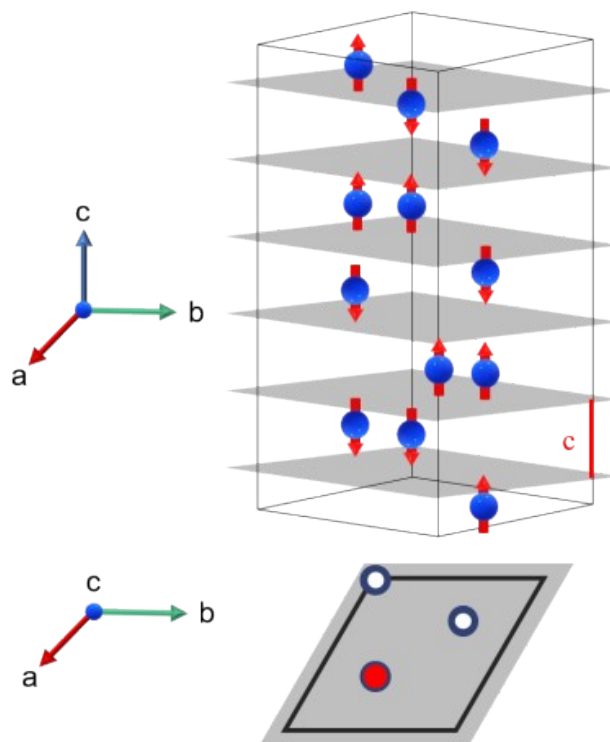


Fig. S1 Schematic representation of the  $\alpha$ - $\text{Fe}_2\text{O}_3$  unit-cell along different axes at the temperature below the Morin transition.<sup>5</sup> Fe atoms are blue balls, and sublattice magnetic moments are red arrows (not to scale).

**Table S1** VAMPIRE program simulated values of saturation magnetization with various thickness

Sample	{001}-3 nm	{001}-4 nm	{001}-5 nm	{001}-6 nm	{001}-7 nm	{001}-8 nm
Ms (emu/g)	13.46	10.29	8.33	7.00	6.03	5.30

### S3: SEM images of {001} samples

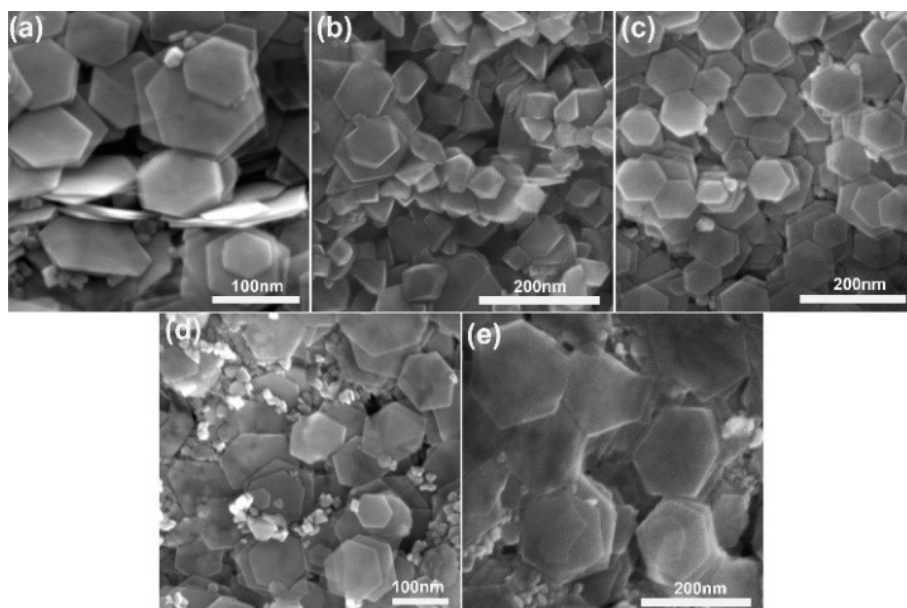


Fig. S2 SEM images of the 5 {001} samples listed in Table 1. (a) {001}-I; (b) {001}-II; (c) {001}-III; (d) {001}-IV; and (e) {001}-V.

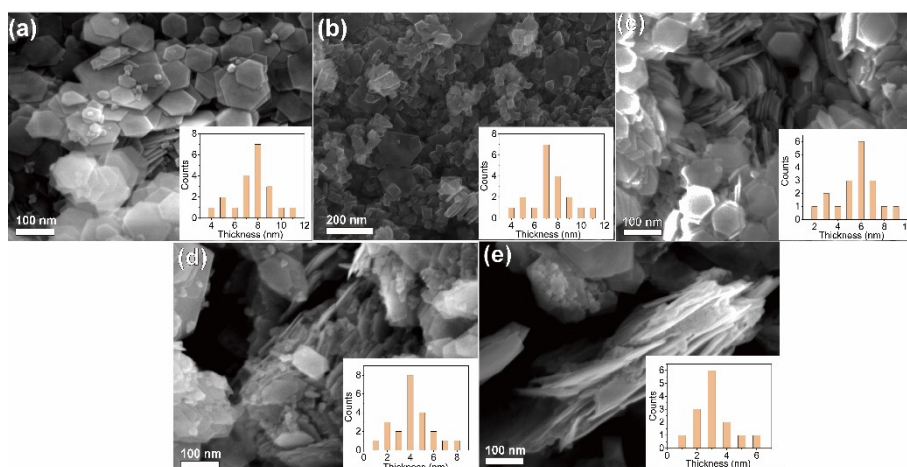


Fig. S3 The SEM images and thickness distribution of nanoplates images of the 5 {001} samples. (a) {001}-I; (b) {001}-II; (c) {001}-III; (d) {001}-IV; and (e) {001}-V.

Fig. S1 shows the typical SEM images of the corresponding  $\{001\}$  samples. It can be seen that these samples are mainly composed by hexagonal-shaped nanoplates. Fig. S2 exhibits the cross sections of these samples. The average thicknesses of these  $\{001\}$  samples are 8 nm, 7.5 nm, 6 nm, 4 nm and 3 nm, for  $\{001\}$ -I,  $\{001\}$ -II,  $\{001\}$ -III,  $\{001\}$ -IV and  $\{001\}$ -V, respectively. We emphasize that although the thickness of the  $\{001\}$  samples deduced from the SEM images could have some minor errors (because it is hardly to get a cross section image of nanoplates from TEM image), the relationship between the thickness and magnetism is qualitatively meaningful.

#### **S4: $^{57}\text{Fe}$ Mössbauer spectra of $\{001\}$ and $\{012\}$ samples.**

To investigate the chemical environment of  $\text{Fe}^{3+}$  and the magnetic interaction, the  $^{57}\text{Fe}$  Mössbauer spectra of the  $\{001\}$ -III and  $\{012\}$  sample were recorded at 300 K and shown in Fig. S3. The spectrum of the  $\{012\}$  sample can be deconvoluted into two spectra, corresponding to the surface disordered  $\text{Fe}^{3+}$ (paramagnetic singlet) and the bulk AFM (sextet), respectively. In contrast, the spectrum of  $\{001\}$ -III can be fitted with one singlet and three sextet, corresponding to the surface disordered  $\text{Fe}^{3+}$ (paramagnetic singlet), the AFM, the surface FM and the interaction between the surface FM and the adjacent AFM, respectively. The fitted value of the  $^{57}\text{Fe}$  Mössbauer spectra are given in Table SII.

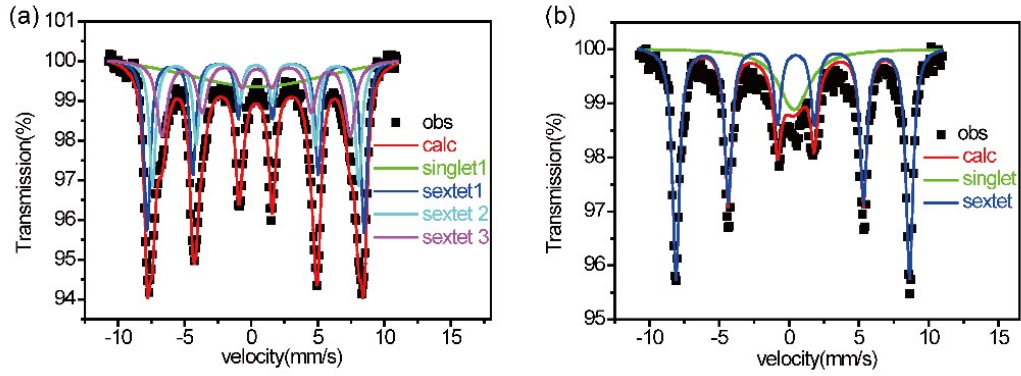


Fig. S4  $^{57}\text{Fe}$  Mössbauer spectra measured at 300 K for  $\alpha\text{-Fe}_2\text{O}_3$  (a)  $\{001\}$ -III, and (b)  $\{012\}$  sample.

**Table S2.** Fitted Mössbauer parameters

Sample	Fitted spectrum	Isomer shift [mm.s <sup>-1</sup> ]	Quadrupole splitting [mm.s <sup>-1</sup> ]	Hyperfine field [kOe]	Percentage [%]
{001}-III	Singlet1	0.480	/	/	40.1
	Sextet1	0.327	0.007	505.0	24.1
	Sextet2	0.340	-0.011	480.1	18.2
	Sextet3	0.393	-0.025	438.5	17.6.
{012}	Singlet	0.350	/	/	22.4
	Sextet	0.380	-0.113	518.8	77.6

### S5: Reported values of saturation magnetization for $\alpha\text{-Fe}_2\text{O}_3$

**Table S3.** Reported values of saturation magnetization and coercive field for  $\alpha\text{-Fe}_2\text{O}_3$ .

Crystal facet (shape)	$M_s$ [emu g <sup>-1</sup> ]	$H_c$ [Oe]	Temperature [K]	Size [nm]	Ref.
{001}-V	14.14	20	300	80*80	This work
{012}	0.85	120	300	30	This work
{012}	0.25	950	300	200	6
{104}	0.48	2.05	300	60	7
{101}	0.05	4986	300	300	8
{101}/{111}	0.04	6512	300	300	8
Spherical	0.45	549	300	60	7

Nanodisc	0.41	214	300	140	9
Cubic	0.24	Not given	300	200	6
Thorhombic	0.6	314	300	300	10
Nanorod	0.55	65	300	50×600	11
Irregular shape	0.6	20	300	40	11
Nanoparticle	6	Not given	300	3-8 nm	12
3D nanoparticle	8.94	Not given	303	20-50	13
2D nanosheets	3-4	Not given	300	Not given	14
{110}					
Nanoparticle	21	20	300	below 5 nm	15
Particle	12.2	95	300	25	16
Thin Films	12	320	300	75-80	17
Thin Films	470 emu/cm <sup>3</sup>	Not given	300	1 μm	18
Thin Films	3.3	Not given	300	10-50 nm	19

### S6: Low temperature and room temperature hysteresis loops

The magnetic hysteresis loop at a low temperature (50 K) was measured and shown in Fig. S5. The hysteresis loops of {001}-III and {001}-V samples were measured at a low temperature of 50 K. Both saturation magnetization  $M_s$  and coercive field  $H_c$  increase at 50 K.

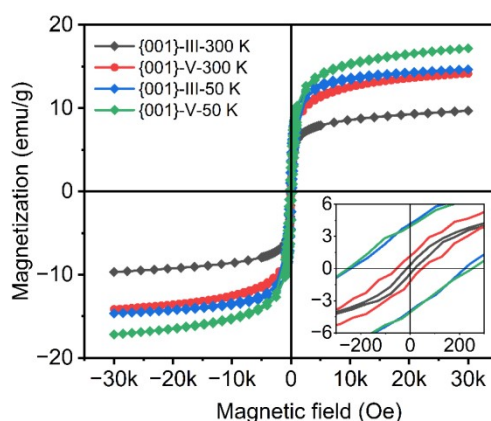


Fig. S5 Magnetization (M) versus magnetic field (H) curves for the {001}-III and {001}-V samples measured at 300 K and 50 K, with the enlarged M-H curves with  $\pm 300$  Oe shown in the insets.

### S7: Curie temperature calculation

We use the Hinze-Nowak Monte Carlo algorithm, using 20000 equilibration steps and 20000 averaging steps, resulting in the calculated temperature-dependent magnetization curves for  $\alpha$ -Fe<sub>2</sub>O<sub>3</sub> shown in Fig. S5. The Curie temperature is calculated to be 675 K.

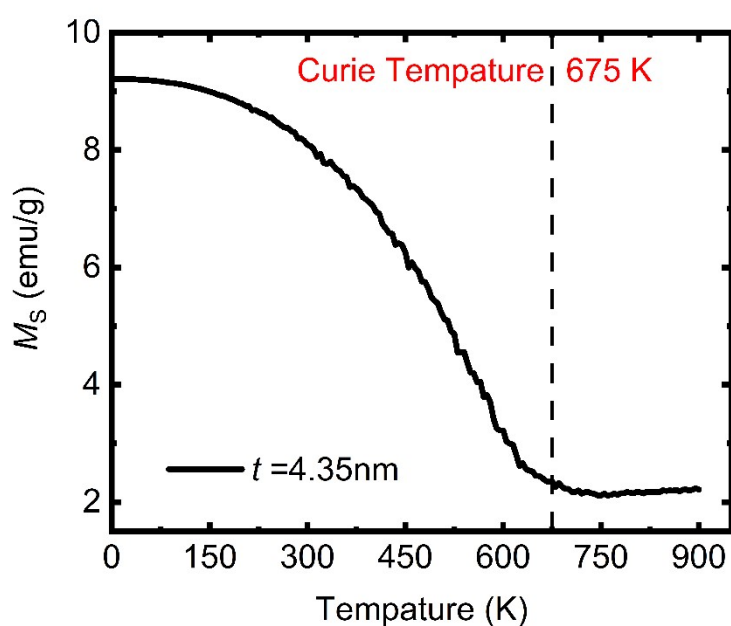


Fig. S6 Calculated temperature-dependent magnetization for the  $\alpha$ -Fe<sub>2</sub>O<sub>3</sub> {001}-IV sample.

### S8: The comparison in ZFC/FC behavior.

**Table S4.** The composition, morphology, ZFC and FC characteristic and mechanism of previous report and this work

Composition, size and morphology	External field	ZFC/FC	ZFC peaks	Explanations	Ref.
$\alpha$ -Fe <sub>2</sub> O <sub>3</sub> nanorods, 25 nm (S600)	1000 Oe	Overlap	T <sub>m</sub> = 224 K	Transition from SPM to spin glass state	20
Porous $\alpha$ -Fe <sub>2</sub> O <sub>3</sub> /Al nanocomposite, 40 nm	100 Oe	T <sub>i</sub> > 350 K; T <sub>B</sub> = 305 K	Broad peak ~305 K	Morin transition was suppressed by porous structure	21

	10 kOe	Overlap	$T_m = 225$ K	-	
$\alpha$ -Fe <sub>2</sub> O <sub>3</sub> {001}-nanoplates 60*60*6 nm.	1000 Oe	$T_i = 240$ K	$T_m = 240$ K; $T_B = 110$ K	Transition from FM to Morin state to SPM	This work
$\alpha$ -Fe <sub>2</sub> O <sub>3</sub> {012}-nanocube		Overlap	$T_m = 220$ K	Transition from WFM to FM	

### S9: Reproducible morphology and magnetic properties of samples.

In order to minimize the experimental deviations, we prepared more than 5 samples for each {001} sample and then characterize its morphology and magnetism properties. Fig. S7 shows the typical SEM, TEM, and M-H properties of {001}-I', {001}-II', and {001}-III' from the different batches of products. It can be seen there are only negligible differences between Fig. S7 and Fig. 1 in the main text. By doing this, we believe these results are reproducible.

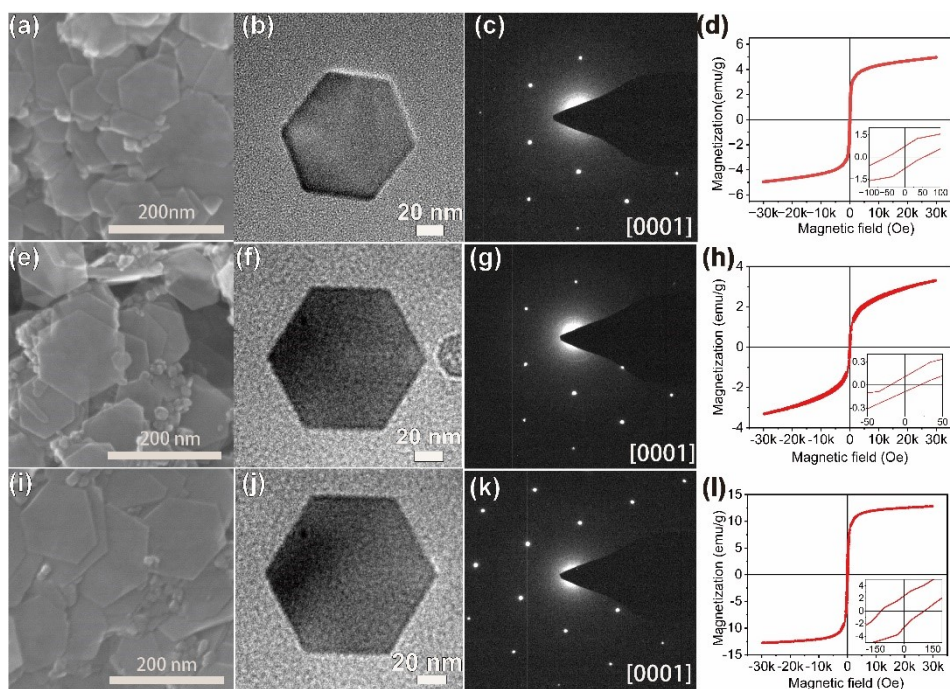


Fig. S7 SEM image, TEM image, SAED pattern and hysteresis loop of {001}-I' sample (a-d), {001}-II' sample (e-h) and {001}-III' sample (i-l).

## References

1. X. Zhou, J. Lan, G. Liu, K. Deng, Y. Yang, G. Nie, J. Yu and L. Zhi, *Angew Chem Int Ed Engl*, 2012, **51**, 178-182.
2. M. Tadic, M. Panjan, V. Damjanovic and I. Milosevic, *Appl. Surf. Sci.*, 2014, **320**, 183-187.
3. A. H. Morrish, *Canted Antiferromagnetism: Hematite*, Canted Antiferromagnetism: Hematite, 1995.
4. D. A. Garanin, *Physical Review B*, 1996, **53**, 11593-11605.
5. H. Jani, J.-C. Lin, J. Chen, J. Harrison and F. Maccherozzi, *Nature*, 2021, **590**, 74-79.
6. R. Liu, Y. Jiang, H. Fan, Q. Lu, W. Du and F. Gao, *Chem. Eur. J.*, 2012, **18**, 8957-8963.
7. Z. Liu, B. Lv, D. Wu, Y. Sun and Y. Xu, *Particuology*, 2013, **11**, 327-333.
8. B. Lv, Z. Liu, H. Tian, Y. Xu, D. Wu and Y. Sun, *Adv. Funct. Mater.*, 2010, **20**, 3987-3996.
9. L. Bao, H. Yang, X. Wang, F. Zhang, R. Shi, B. Liu, L. Wang and H. Zhao, *J. Cryst. Growth*, 2011, **328**, 62-69.
10. W. Wu, S. Yang, J. Pan, L. Sun, J. Zhou, Z. Dai, X. Xiao, H. Zhang and C. Jiang, *CrystEngComm*, 2014, **16**, 5566-5572.
11. J. Lian, X. Duan, J. Ma, P. Peng, T. Kim and W. Zheng, *ACS Nano*, 2009, **3**, 3749-3761.
12. L. Kopanja, I. Milosevic, M. Panjan, V. Damjanovic and M. Tadic, *Appl. Surf. Sci.*, 2016, **362**, 380-386.
13. Y. Sui, F. Lu, X. Liu, Y. Zhang, X. Sun and C. Liu, *Phys. Lett. A*, 2021, **408**, 127488.
14. J. Mohapatra, A. Ramos, J. Elkins, J. Beatty, M. Xing, D. Singh, E. C. La Plante and J. Ping Liu, *Appl. Phys. Lett.*, 2021, **118**, 183102.
15. K. V. Manukyan, Y.-S. Chen, S. Rouvimov, P. Li, X. Li, S. Dong, X. Liu, J. K. Furdyna, A. Orlov, G. H. Bernstein, W. Porod, S. Roslyakov and A. S. Mukasyan, *J. Phys. Chem. C*, 2014, **118**, 16264-16271.
16. J. Wu, S. Mao, Z.-G. Ye, Z. Xie and L. Zheng, *ACS Appl. Mater. Interfaces*, 2010, **2**, 1561-1564.
17. S. Robbenolt, A. Nicolenco, P. Mercier Fernandez, S. Auffret, V. Baltz, E. Pellicer, E. Menéndez and J. Sort, *ACS Appl. Mater. Interfaces*, 2019, **11**, 37338-37346.
18. A. Akbar, S. Riaz, M. Bashir and S. Naseem, *IEEE Trans. Magn.*, 2014, **50**, 1-4.
19. F. F. H. Aragón, J. D. Ardisson, J. C. R. Aquino, I. Gonzalez, W. A. A. Macedo, J. A. H. Coaquira, J. Mantilla, S. W. da Silva and P. C. Morais, *Thin Solid Films*, 2016, **607**, 50-54.
20. M. Tadic, M. Panjan, Y. Lalatone, I. Milosevic, B. V. Tadic and J. Lazovic, *Adv. Powder Technol.*, 2022, **33**, 103847.
21. M. Tadic, M. Panjan, B. V. Tadic, S. Kralj and J. Lazovic, *Ceram. Int.*, 2022, **48**, 10004-10014.